Polarization Resolved bP / MoS₂ Mid-Wave Infrared Photodiodes with High Detectivity at Room Temperature

James Bullock[1,2‡], Matin Amani[1,2‡], Joy Cho[1,2], Yu-Ze Chen[3], Geun Ho Ahn[1,2], Valerio Adinolfi[1,2], Vivek Raj Shrestha[4], Yang Gao[5], Kenneth B. Crozier[4,5], Yu-Lun Chueh[3] and Ali Javey[1,2,*]

[1]*Department of Electrical Engineering and Computer Sciences, University of California, Berkeley, California 94720, USA.*

[2]*Materials Sciences Division, Lawrence Berkeley National Laboratory, Berkeley, California 94720, USA.*

[3]*Department of Materials Science and Engineering, National Tsing Hua University, Hsinchu, Taiwan 30013, R.O.C.*

[4] *School of Physics, University of Melbourne, VIC 3010, Australia*

[5] *Department of Electrical and Electronic Engineering, University of Melbourne, VIC 3010, Australia*

‡ *These authors have contributed equally to this work*

* *corresponding author: Ali Javey (ajavey@berkeley.edu)*

Infrared (IR) photodetectors are currently subject to a rapidly expanding application space, with an increasing demand for compact, sensitive, and inexpensive detectors. Despite continued advancement, technological factors limit widespread usage of IR detectors; specifically, the need for cooling and high costs associated with processing of III-V/II-VI semiconductors. Here, black-phosphorous (bP) / MoS_2 heterojunction photodiodes are explored as mid-wave infrared (MWIR) detectors. While previous studies have demonstrated photodiodes using bP, here we significantly improve the performance, showing for the first time that such devices can be competitive with conventional MWIR photodetectors. By optimizing the device structure and light management, we demonstrate a two-terminal device which obtains room temperature external quantum efficiencies (η_e) of 35% and specific detectivities (D^*) as high as 1.2×10^{10} cmHz$^{1/2}$W^{-1} in the MWIR region. Furthermore, by leveraging the anisotropic optical properties of bP we demonstrate the first bias-selectable polarization resolved photodetector which operates without the need for external optics.

Infrared (IR) photodetectors are essential components in a host of fields, including medical, scientific, communication, automation and surveillance.[1,2] The majority of today's commercially available, high performance IR photodetectors are made using III-V and II-VI absorbers, for example, $In_{1-x}Ga_xAs$, InSb, and $Hg_{1-x}Cd_xTe$.[3] While significant progress has

2

39greatly increased their application, a number of drawbacks limit wider

40utilization of IR photodetectors. Most notably, these devices typically rely on

41expensive growth methods and require active cooling to reduce thermal

42noise. The latter is particularly crucial for narrow bandgap absorbers

43operating in the mid-wave infrared (MWIR, 3-5 μm) and long wave infrared

44(LWIR, 8-12 μm) spectral bands where cryogenic cooling is typically required

45to achieve high performance. In addition, several specific applications cannot

46be directly addressed using detectors fabricated from traditional material

47systems. An example of this is detection of the polarization state of light,

48which is utilized in numerous specialized applications including astronomy,

49polarization-division multiplexing and remote sensing. Normally detectors

50used for this application require either polarization optics or multiple devices

51arranged in a side-by-side configuration, which adds system complexity and

52limits the resolution for imaging purposes. Furthermore, while numerous

53materials, most notably nanowires, show polarized absorption, a polarization

54resolved detector has yet to be demonstrated. As such, there is considerable

55interest in the exploration of new IR absorber materials which offer the

56potential to address these shortcomings and can be applied in novel device

57architectures.

58   Two-dimensional (2D) materials have shown initial promise for use in

59future IR photodetectors.[4,5] One of the key advantages offered by 2D layered

60crystals is their out-of-plane van der Waals bonding which allows the use of

61thin layers without suffering from detrimental effects such as surface

62 dangling bonds. This advantage is particularly important in infrared detectors
63 where thin absorbers can reduce noise resulting from generation-
64 recombination, a strategy which is often not permitted in traditional
65 semiconductors due to surface recombination. Furthermore, the van der
66 Waals bonding in these materials allows for the construction of
67 heterojunctions without consideration of factors such as lattice matching or
68 deposition temperature; providing a significant advantage over traditional
69 three-dimensional materials. Black phosphorus (bP), an elemental 2D
70 material, has recently garnered a significant amount of attention within the
71 optoelectronic community.[5-7] This interest is partially based on the
72 anisotropic optoelectronic properties of bP, which result in polarization
73 dependent absorption.[7,8] Black phosphorus also exhibits a thickness tuneable
74 direct bandgap, between the near infrared ($E_g \approx 1.5$ eV) for monolayers to
75 the MWIR ($E_g \approx 0.3$ eV) in the case of bulk.[7,8] In addition, several studies have
76 demonstrated that bP can be effectively combined with transition metal
77 dichalcogenides including MoS_2,[9-11] WSe_2,[12] and ReS_2,[13] to form a range of
78 functional van der Waals heterojunctions. To date, numerous photodetectors
79 utilizing bP have been demonstrated indicating its promise as a next-
80 generation IR detector platform.[14-16] Among these, a number of preliminary
81 studies have shown the potential of the bP / MoS_2 heterojunction in this
82 application.[9-11] However, devices presented thus far show inferior
83 performance to existing IR room temperature photodetectors, with reported
84 external quantum efficiency values of less than 5%; and are characterized

85only at discrete wavelengths either in the near infrared or short-wave

86infrared bands.

87   Here we utilize bP / MoS_2 heterostructures to fabricate photodiodes and

88optimize the devices for detection of MWIR light intensity and polarization at

89room temperature. To optimize the collection of light, we perform in-depth

90characterisation of bP, and report, for the first time, the complex refractive

91index of this material in a wavelength range that encompasses the MWIR.

92This information is used to design and fabricate a simple optical structure

93which deliberately utilizes destructive interference to efficiently couple in a

94narrow band of MWIR light – permitting the demonstration of a high quantum

95efficiency bP / MoS_2 photodiode. Finally, we demonstrate a bias-selectable

96polarization resolved bP photodetector, utilizing two orthogonally aligned bP /

97MoS_2 photodiodes, monolithically integrated to create a device which directly

98measures both the intensity and polarization of incoming MWIR light.

99**Results and discussion**

100   **Black phosphorus mid-wave infrared photodiode design.** Two

101primary figures of merit for photodetectors are their external quantum

102efficiency (η_e) and specific detectivity (D^*). These parameters are optimized

103by increasing the percentage of incident photons which generate

104photocurrent as well as via reduction of the electronic noise. As such,

105simultaneous optimization of η_e and D^* requires consideration of both optical

106and electrical design. A schematic showing the structure of the

107heterojunction photodiodes fabricated in this work as well as an example
108optical micrograph are shown in Fig. 1a and 1b, respectively. The device
109consists of a bP / MoS$_2$ heterojunction where a thin (~10-20 nm) n-type MoS$_2$
110layer acts as an electron selective-contact and MWIR window. Holes are
111contacted via a rear Au pad, which simultaneously acts as a MWIR back
112reflector. As shown schematically in the simulated band diagram of Fig 1c,
113the MoS$_2$ heterojunction provides asymmetric band offsets with the bP,
114allowing the flow of electrons to the MoS$_2$ contact while blocking the flow of
115holes. A false coloured transmission electron micrograph (TEM) of a
116completed device is shown in Fig. 1d. In addition, high resolution TEM images
117of the bP / MoS$_2$ and bP / Au interfaces are shown in Fig. 1e and 1f,
118respectively. The layered structure of bP and MoS$_2$ can be seen with
119corresponding monolayer thicknesses of 5.5 Å and 6 Å, respectively. A thin
120amorphous layer can also be observed at both interfaces, most prominently
121at the bP / Au interface, and is attributed to PO$_x$ which forms during device
122fabrication. This layer could potentially improve hole collection at the bP / Au
123interface because of its known p$^+$ character which may reduce the hole
124contact resistivity. However, its growth at the bP / MoS$_2$ interface would
125ideally be avoided to prevent the formation of an electron barrier which
126could result in a reduced collection efficiency.

127   **Refractive index extraction and optical optimization.** Losses due
128to reflection limit the fraction of incident light that can be absorbed and are a
129strong function of both the bP and MoS$_2$ layer thicknesses. The reflection and

130 absorption in the device can be modelled utilizing the complex refractive 131 index (n, k) of the two materials. While broadband values of n and k have 132 been reported for MoS_2, only the visible refractive index has been 133 characterized for bP to date.[17] The anisotropic crystalline structure of bP, 134 shown in Fig 2a, results in polarization dependent optical properties (referred 135 to as linear dichroism). Light impinging with an electrical field parallel to the 136 x-axis, or arm-chair direction, sees a sharp absorption onset at the bulk bP 137 band edge of ~0.31 eV.[6,7,18] Absorption of polarized light aligned to the y-138 axis or zig-zag direction, however, is symmetry-forbidden at the ~0.31eV 139 band edge and substantially weaker at higher energy wavelengths.[7,8,19] This 140 has been confirmed experimentally for bulk bP from MWIR to visible 141 wavelengths.[5,7,20] To extract an effective n and k for the x-and y-directions in 142 bP, polarized IR reflection measurements were performed on bP crystals with 143 varying thickness, ranging from 50 nm to 500 nm, on Au substrates. Example 144 reflection data at individual thicknesses is included in Supplementary 145 Information S1. The combined interpolation of these polarized reflection 146 measurements is shown in Fig. 2b and 2c for incident polarisations aligned 147 along the x- and y-axis of bP, respectively.

148   For polarized illumination aligned to the x-direction, a clear drop in 149 reflection can be seen at photon energies above 0.31 eV for all thicknesses. 150 This is a result of the onset of absorption at the band edge of bP. As 151 expected, no such sharp step is seen for the y-direction in Fig. 2c. Refractive 152 index values are obtained using the transfer matrix method[17] to fit a model

153of the thickness (t) dependent reflection $R_{model}(t)$ to the measured reflection

154$R_{meas}(t)$ at each wavelength. The model is based on a bP / Au stack and

155assumes that the refractive index is thickness independent across the

156measured thickness range (50 – 500 nm). This assumption is based on the

157predicted saturation of the layer dependent band-structure of bP above ~8

158layers,[6] and also further demonstrated by fitted reflection measurements in

159Supplementary Material S1. The extracted n and k values for the x-direction

160and y-direction are provided in Fig. 2d and 2e, respectively. For light

161polarized in the x-direction a pronounced step in the extinction coefficient, k,

162is observed at $\lambda = 3.8$ µm which corresponds well to the expected band edge

163of bP. More details of the indices extraction process can be found in

164Supplementary Material S1.

165   With these n and k values, we use the transfer matrix method to

166simulate the absorption of the photodiode in the x-direction. Ideally from an

167electrical standpoint, the thickness of the bP layer should be minimized in

168order to reduce noise resulting from generation-recombination as well as to

169improve the carrier extraction efficiency. However, from an optical

170perspective, absorption within the bP layer, which is small for very thin

171layers, should be maximised. To obtain a compromise between these two

172requirements, the bP absorption, averaged between $\lambda = 2.5\text{-}3.8$ µm, is

173simulated as a function of the bP and MoS_2 layer thicknesses. A contour plot

174of the modelled absorption is provided in Fig. 2f. The periodic absorption

175behaviour is associated with changes in front surface reflection due to

176thickness dependent constructive and destructive interference of MWIR light.

177A local maximum in absorption is seen for bP layers with a thickness of 170

178nm on Au, with an MoS_2 thickness of zero. This corresponds to the expected

179quarter wavelength minima in reflection, and hence interference effects can

180be used to provide a compromise between minimising thickness and

181maximising absorption. Given that an MoS_2 layer with sufficient lateral

182conductivity is required to collect electrons, we choose an optimum device

183configuration of bP (~150 nm) / MoS_2 (15 nm). With this optical design ~80%

184of incident light polarized in the x-direction at $\lambda = 3$ µm can be absorbed in

185the bP layer. We emphasize that, in terms of device thickness, this detector

186bridges the gap between conventional 2D material photodetectors and

187traditional bulk semiconductor detectors. Resultantly, it inherits benefits

188from both of these two detector classes, such as increased absorption as well

189as being free of surface dangling bonds.

190   **Photodiode characterization.** The *IV* characteristics of a typical bP /

191MoS_2 heterojunction photodiode, measured at 300 K with no illumination, is

192provided in Fig. 3a and shows the expected rectifying behaviour of a diode

193formed using a narrow bandgap material. The inset of Fig. 3a compares the

194measured *IV* behaviour with and without illumination from a 1000 K

195unpolarized blackbody source. The generation of photocarriers shifts the *IV*

196curve downwards, resulting in an open circuit voltage V_{oc} and short circuit

197current I_{sc}, confirming that the device is operating in the photovoltaic mode.

198Figure 3b shows the relationship between the short circuit current density J_{sc}

199and incident optical power density from a $\lambda = 2.7$ μm laser diode source. The

200device shows the expected linear increase in photocurrent as a function of

201incident light power density over the full measurement range, which spans

202five orders of magnitude. Similar results are found using a $\lambda = 1.6$ μm

203illumination source as shown in Supplemental Information S5.

204   The quantum efficiency of the device is measured under *x*-direction

205polarized illumination using a calibrated Fourier transform infrared

206spectrometer (FTIR), the setup of which is described in the Methods section.

207As shown in Fig 3c, the bP / MoS$_2$ photodiode shows an external quantum

208efficiency η_e of ~30-35% from λ=2.5-3.5 μm. These are the highest η_e values

209reported for bP in this range at room temperature and correspond to current

210responsivity values of ~0.9 A/W (see Supplemental Information S3). Also

211presented in Fig 3c is the measured reflection *R*, plotted as 100%-*R*. The

212narrow spectral band of MWIR light coupled into the absorber corresponds to

213the targeted quarter wavelength interference feature with its peak occurring

214just below λ=3 μm. From η_e and *R,* the internal quantum efficiency (η_i) can

215also be calculated according to: $\eta_i(\lambda)=\eta_e(\lambda)/¿$), yielding a value of 40-50% at

216room temperature. The polarization dependence of η_e at λ = 3.5 μm, as a

217function of polarization angle, is provided in the polar plot of Fig. 3d. It can

218be seen that as the polarization angle is changed from 0° (aligned with the *x*-

219axis) to 90° (aligned to the *y*-axis) a decrease in η_e, from greater than 30% to

220less than 1%, is measured. An example $\eta_e(\lambda)$ comparison, across the MWIR

221spectral range, for these two polarization angles is included in the

222Supplementary Information S3. That the η_e for *x*-polarized light is 223substantially higher than for *y*-polarized light is consistent with the 224anisotropic absorption discussed in Fig. 2 and is in alignment with previous 225responsivity measurements of bP photodetectors at shorter wavelengths.[7]

226   As shown in Fig. 3e, the η_e shows no significant changes in spectral 227shape as a function of temperature, apart from a small red-shift in the 228absorption edge, attributed to a decrease in the bandgap with decreasing 229temperature. This anomalous temperature dependence of the bandgap has 230been previously predicted and experimentally observed in bP.[18,19] However, 231η_e increases as the temperature is decreased, reaching a value of 63% at 78 232K. This is further illustrated in the inset of Fig 3c, with η_e and η_i (measured at 233λ = 3 μm) plotted as a function of inverse temperature, showing that η_i 234reaches a peak value of 84% at 100 K. This is most likely a result of an 235increase in the minority carrier diffusion length at lower temperature. For a 236device where the back contact is several minority carrier diffusion lengths 237(L_d) away from the junction, the internal efficiency can be calculated using:

238
$$\eta_i = \left(1 - R(\lambda)\right)\frac{\alpha(\lambda)L_d}{1 + \alpha(\lambda)L_d} \qquad (1)$$

239where α is the absorption coefficient. The increase in η_i from 300 K to 77K 240observed here, is consistent with Hall mobilities measured for bP ($\mu_{h,300k}$ ≈ 241750 cm^{2}V^{-1}s^{-1}, $\mu_{h,77k}$ ≈ 3,800 cm^{2}V^{-1}s^{-1}).[24]

242   To directly compare the performance of the bP / MoS$_2$ photodiode to 243conventional photodetectors, we extract its specific detectivity D*. This is 244achieved utilizing two independent approaches, which are discussed in detail 245in the Methods section. Firstly, D* is calculated, following the approach 246suggested in Ref[3] for a photodiode under 0 V bias, from η_e and the zero-bias 247resistance area product (R_0A):

248
$$D^{*}=\frac{\eta_e \lambda q}{hc}\left[\frac{4kT}{R_0 A}+2q^2\eta_e\Phi_b\right]^{-1/2}$$
(2)

249where λ is the wavelength, q is the elementary charge, c is the speed of light 250in vacuum, T is the detector temperature, Φ_b is the background flux density 251and h and k are the Planck and Boltzmann constants. The second term in the 252parenthesis accounts for contributions to noise from fluctuations in the 253thermal background and is negligible in this case, since $4kT/R_0A > 2q^2\eta\Phi_b$. 254Figure 3f shows D*(λ) extracted from this approach at room temperature 255compared against the current state-of-the-art room temperature 256photodiodes,[21,22] many of which are commercially available. It can be seen 257that the bP photodiode outperforms more established technologies in the 258MWIR region, with a peak D* of 1.2×10^{10} cmHz$^{1/2}$W^{-1} at λ = 3.8 μm. It should 259be noted that the MoS$_2$ / bP photodiode presented in Figure 3 has been 260characterized at 0 V bias, unlike many of the detectors presented in Figure 2613f, which require an applied bias to obtain the reported values. To verify the 262MoS$_2$ / bP photodiode D* values, the noise equivalent power (NEP) was 263measured for this device under flood illumination from a blackbody source as

264described in Supplementary Information S4. In this approach the incident

265power density is calculated using geometrical considerations, the

266temperature of the source and an integration of the total irradiance to the

267band edge.[23] Additionally, the noise is directly measured allowing $D*$ to be

268calculated as $\sqrt{A\,\Delta f}/NEP$, where Δf is the integration time (1 second). From

269this measurement, we find a room temperature $D*$ value of 7×10^9 cmHz$^{1/2}$W^{-1}

270. This value is in good agreement with the spectral $D*$, calculated from the

271device R_0A shown in Fig. 3f. Further information on the $D*$ for these

272detectors, including its temperature dependence, can be found in

273Supplementary Information S3 and S4.

274 The frequency response and noise current for the bP / MoS$_2$

275heterojunction photodiodes is characterized in Fig. 4. As shown in Fig. 4a no

276observable baseline drift in photoresponse is observed under modulated

277laser diode illumination (λ = 2.7 μm). In addition, the rise and fall times,

278measured under λ = 2.7 μm illumination at 0 V bias, are found to be 3.7 μs

279and 4 μs, respectively as shown in Fig. 4b. These values are among the

280fastest reported for bP based photoconductors and photodiodes.[13,15,24] While

281this is slower than commercially available MWIR photodiodes,[29] these values

282are promising given the early stage of device development and are faster

283than common photoconductive and thermal detectors, as shown in

284Supplementary Table S2. The dashed purple lines in Fig. 4b, measured from

285a commercially available InAs photodiode, are included to provide a

286reference of the instrument response. Similar rise / fall times are found when

287an illumination source of $\lambda = 1.6$ μm is used, as shown in Supplementary

288Information S5. Figure 4c shows the measured frequency response, with the

2893 dB point at approximately 100 kHz using a $\lambda = 1.6$ μm illumination source.

290Fig. 4f shows the measured noise current spectrum of the bP / MoS$_2$

291photodiode. The shape it exhibits is commonly seen in systems dominated

292by generation-recombination noise. Notably $1/f$ noise behaviour is not

293observed at low frequencies since the device is operated in photovoltaic

294mode at zero bias.[30]

295   **Polarization-resolved, bias-selectable photodetector.** Finally, we

296leverage this device structure and the anisotropic optical properties of bP to

297develop a polarization resolved detector. A schematic of the polarization

298resolved detector developed in this study is shown in Fig. 5a and a false

299coloured TEM cross-section of a fabricated device is shown in Fig. 5b. The

300device consists of two vertically stacked bP layers arranged so that their

301crystal orientations are perpendicular to one another. These two bP layers

302are separated by a common MoS$_2$ electron contact and each bP layer has an

303isolated hole contact. This configuration is similar to two-colour back-to-back

304photodiodes which have been previously demonstrated with III-V

305semiconductors.[31] The bottom bP layer utilizes a full-area Au hole contact,

306similar to the photodiodes presented above, while the top bP layer collects

307holes through a MoO$_x$ / Pd hole contact adjacent to the back reflector. The

308MoO$_x$ / Pd stack has been shown to be an effective hole contact to a number

309of semiconductor materials,[32,33] owing to its large work function.

310   To demonstrate the performance of this device, spectrally resolved

311photoresponse measurements are taken individually on the top and bottom

312bP photodetectors using the circuit configuration shown in Fig 5c *i* and *ii*,

313respectively. Each device is measured under two conditions: linearly

314polarized light aligned to the *x*-axis of the top device (90°) and, linearly

315polarized light aligned to the *x*-axis of bottom device (0°). All four

316measurements are provided in Fig. 5d. The performance of this device can

317be quantified by an extinction ratio r_e for each layer, defined as the

318photoresponse measured with *x*-polarized illumination divided by

319photoresponse for *y*-polarized illumination. For both the top and bottom

320devices r_e values of ~100:1 are calculated at $\lambda = 3.5$ μm, which is on the

321order of the extinction ratio of the polarizer used in this study. These results

322are further corroborated by the polar plot of Fig. 5e, which shows the

323photoresponse as a function of polarizer angle at $\lambda = 3.5$ μm. In separate

324measurements, presented in Supplementary Information S6, it is shown that

325the device is also able to simultaneously detect the two linear polarization

326components when illuminated with unpolarized light. Furthermore, the

327response from the individual detectors can be accessed in a bias-selectable

328(*i.e.* two-terminal configuration) as depicted in the circuit schematic of Fig 5c

329*iii*. By applying a bias of ±250 mV across the outer contacts one device is

330reverse biased (where the photocurrent is collected), and the other forward

331biased (contributing negligibly to the photocurrent). Note that for these

332measurements the MoS_2 contact was electrically disconnected. The

333functionality of this configuration is clearly seen in Fig. 5f by the exclusive 334collection of only 0° or 90° linear polarized MWIR light under negative or 335positive biasing, respectively. A bias of ±250 mV was chosen as it was the 336minimum value at which photocurrent from the two detectors could be 337effectively separated. Higher biases were avoided to minimise noise due to 338dark current in the device. The unbalanced photocurrent from the top and 339bottom bP layers can be attributed to a combination of device variation and 340differences in absorption arising from the layer thicknesses and their position 341within the device stack. An optical structure, which couples in and absorbs 342an equal proportion of perpendicularly polarized light in the two bP 343absorbers, can be realized by controlling the bP and MoS_2 layer thicknesses 344and integrating an antireflection layer.

345**Conclusion**

346   In summary, we have designed and fabricated MWIR bP / MoS_2 347heterojunction photodiodes with high performance at room temperature. By 348determining the complex refractive index in the IR, we have designed a 349simple optical structure for the bP / MoS_2 photodiode that achieves high 350MWIR absorption via interference. This allows the use of a moderately thin bP 351layer (~150 nm), which reduces noise while still permitting high absorption 352(in excess of ~80%) within a narrow band in the MWIR region. These devices 353display impressive room temperature η_e and D^* values of 35% and 1.2×10^{10} 354$cmHz^{1/2}W^{-1}$, respectively. Finally, we utilize the anisotropic optical properties 355of bP to demonstrate a bias-selectable polarization-resolved monolithic

356photodetector, which is capable of simultaneously detecting orthogonally

357polarized light without the use of external optics. This could further be

358expanded upon to create polarimetry focal plane arrays which do not rely on

359moving parts or additional optical components.

360**Methods**

361**Refractive index extraction and optical simulations.** Samples for

362refractive index extraction were fabricated by thermally evaporating Ti / Au

363(5/80 nm) onto a Si/SiO$_2$ carrier wafer. Following this, bP (Smart Elements)

364was mechanically exfoliated onto the Au surface in an N$_2$ purged glovebox. A

365set of 22 bP flakes were chosen with approximately linearly spaced thickness

366from 50 to 500 nm, as measured by atomic force microscopy (AFM) (Bruker

367Dimension Icon). Polarized reflection measurements were taken using a

368Fourier transform infrared (FTIR) microscope (Thermo Scientific, Nicolet iS50)

369with a BaF$_2$ wire grid linear polarizer (Thorlabs). The arm-chair direction of

370the bP absorber was determined by measuring reflection as a function of

371polarization, to find the angle at which maximum absorption occurs. Implicit

372in this approach is the assumption that the largest absorption will occur

373when light is aligned to the *x*, or arm-chair direction, a fact that has been

374theoretically predicted and demonstrated by a number of previous

375studies.[7,34,35] In all cases the minimum absorption (at 0.31 eV) was found to

376be offset by 90° from this angle, corresponding to the expected zig-zag or *y*-

377direction. All FTIR reflection measurements in this study utilize a bare Au

378surface as a 100% reflection standard. The set of reflection curves in the *x*-

379direction were fitted using the transfer matrix method, which models the

380reflection of the bP / Au stack using the refractive indices of bP as the only

381fitting parameter. The optical simulations of the full bP / MoS$_2$ / Au

382photodiodes were also performed through the transfer matrix method

383utilizing known refractive index values for Au, constant values for MoS$_2$ ($n =$

3844.3, $k = 0$), as well as the refractive index values for bP measured in this

385work. An average of the bP absorption values over the $\lambda = 2.5$-3.8 µm range

386was obtained for every combination of MoS$_2$ and bP thicknesses.

387**Device fabrication.** Photodiodes presented in this work were fabricated by

388a dry transfer process utilizing a poly(methyl methacrylate) (PMMA) carrier. A

389detailed description of this process can be found in Supplemental

390Information S2. In brief, freshly exfoliated bP and MoS$_2$ sheets are transferred

391onto an Au pad creating an Au / bP / MoS$_2$ stack. A contact to the MoS$_2$ layer

392was then patterned by e-beam lithography and a 40 nm thick Ni film was

393subsequently deposited by thermal evaporation. In some devices, the

394heterojunction was patterned by e-beam lithography and subsequently

395etched in a Xactix vapor etching tool by XeF$_2$.[36] Finished devices were

396encapsulated by an ~2 nm thick AlO$_x$ layer formed by thermal evaporation of

397Al. Example micrographs taken during the above process steps is provided in

398Supplementary Figure S2. A discussion of the assumptions made for the area

399of the device is provided in Supplementary Information S2.

400For the polarization resolved detector, an identical dry transfer process was

401used to create an MoS$_2$ / bP / Au stack. An additional bP flake was transferred

402on top of the MoS$_2$ layer such that its crystal orientation was orthogonal to
403the bottom bP layer. The crystalline orientations of the bP sheets was
404determined using polarized reflection measurements performed in an FTIR
405microscope as described above. The hole contact for the top bP device was
406patterned using electron beam lithography, followed by evaporation of
407MoO$_x$ / Pd (4/30 nm). For all devices in this study, care was taken to reduce
408air exposure during fabrication of devices to minimize PO$_x$ growth at the bP
409surface. Processing steps including bP exfoliation, lift-off, PMMA removal and
410AFM were all performed in either a glovebox or a nitrogen purged
411environment and all chemicals used were anhydrous. For measurements of
412surface oxidation prevention in fabricated devices please see Supplementary
413Information S3.

414**Device characterisation.** Finished devices were wire-bonded into 24 pin
415chip-carriers which were in turn mounted into a cryostat with a CaF$_2$ window
416and measured at a base pressure < 10^{-5} Torr. Current-voltage measurements
417were taken in a 2-probe configuration, under vacuum using an Agilent
418Technologies B1500A semiconductor device analyser. Spectral response and
419η_e were characterized at I_{sc} (i.e. 0 V bias) by placing the cryostat at the
420auxiliary exit port of the FTIR. The sample was then excited using modulated
421illumination from a Globar (1000 K blackbody). The resulting photocurrent
422was then sent to a current amplifier (Stanford Research Systems SRS570)
423and subsequently returned to the external detector interface of the FTIR. For
424polarization resolved measurements, a BaF$_2$ wire grid linear polarizer was

425placed in the beam path. The FTIR system was calibrated using two
426reference detectors: a NIST calibrated Ge photodiode is used to measure the
427source intensity at the outlet and an inbuilt deuterated-triglycine sulfate
428(DTGS) detector is used to measure the relative spectral intensity of the
429source. Further information on the FTIR setup is provided in Supplementary
430Information S3. Additionally, the detectivity values are confirmed using a
431blackbody setup with flood illumination. Here the device is excited using a
432chopper-modulated blackbody (temperature range 473 to 673 K) with no
433additional optics besides the cryostat window; the incident power density
434here is calculated using Planck's law and geometrical considerations, *i.e.*
435aperture size and sample to blackbody distance. Further details on this
436process can be found in Supplementary Information S4 and in Ref.[23]
437Reflection measurements are performed in an attached FTIR microscope,
438with the wire grid polarizer placed in the incoming beam path. The rise/fall
439times and linearity of the device were characterized using illumination from a
440λ = 2.7 µm laser diode. For rise/fall measurements the laser diode was
441directly modulated with a square waveform, and the instrument response
442was measured using a commercial InAs photodiode. For frequency response
443measurements a SRS570 current amplifier in high-bandwidth mode with a
444gain >20 µA/V was used (corresponding to a bandwidth of 1 MHz). For
445dynamic range measurements the laser was directly modulated at a
446frequency of 120 Hz. The photocurrent was measured using a lock-in
447amplifier (Stanford Research Systems SR865). The laser diode intensity was

448adjusted over a five order of magnitude dynamic range by controlling the

449laser current in combination with the use of neutral density filters in the

450beam path. The 3dB frequency analysis was performed with a $\lambda = 1.6$ μm

451laser diode, directly modulated with a sinusoidal waveform.

452AUTHOR INFORMATION

453**Corresponding Author**

454*E-mail: ajavey@berkeley.edu

463**Author Contributions**

464J.B., M.A. and A.J. conceived the idea for the project and designed the 465experiments. J.B. and M.A. performed optical measurements. M.A., J.B., J.C., 466and G.H.A. fabricated devices. V.A. performed device simulations. Y.-Z.C. and 467Y.-L.C. performed TEM measurements. J.B, M.A., V.A., V.R.S., Y.G., K.B.C. and 468A.J. analysed the data. J.B., M.A., and A.J. wrote the manuscript. All authors 469discussed the results and commented on the manuscript.
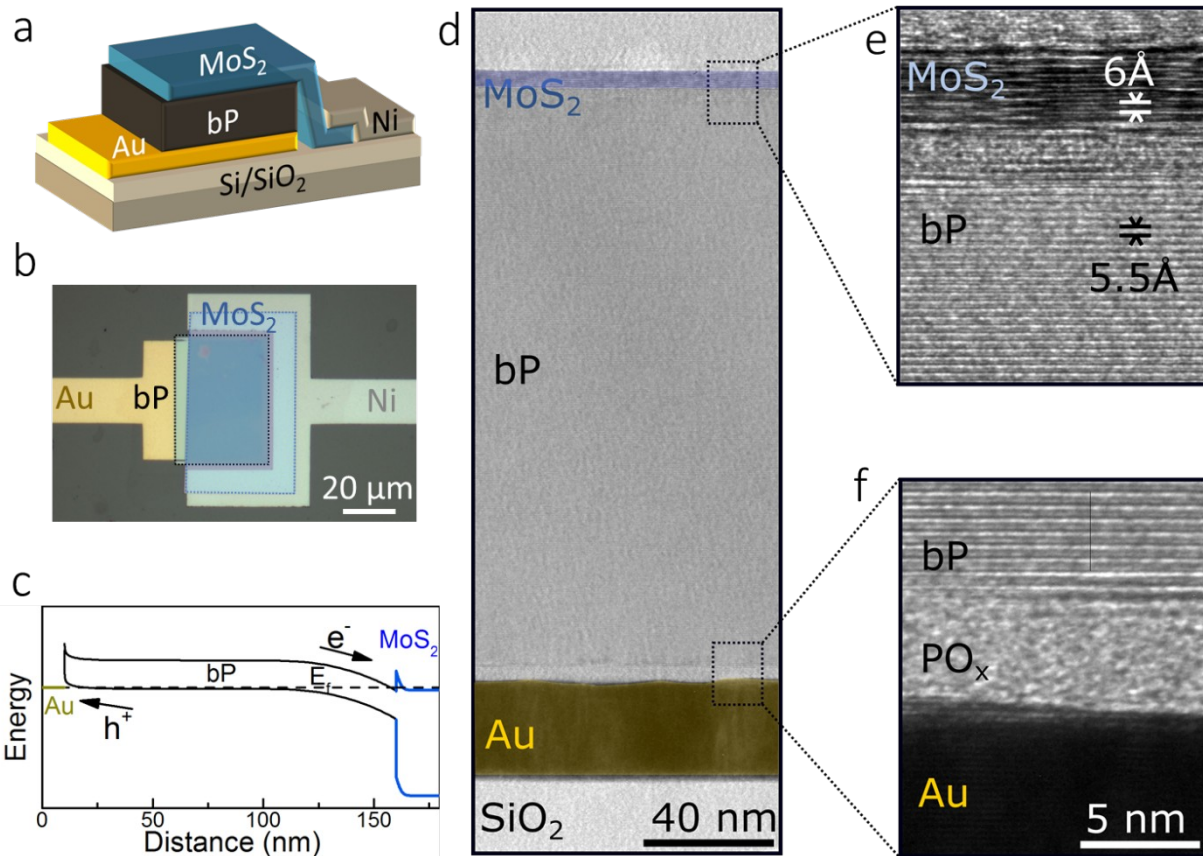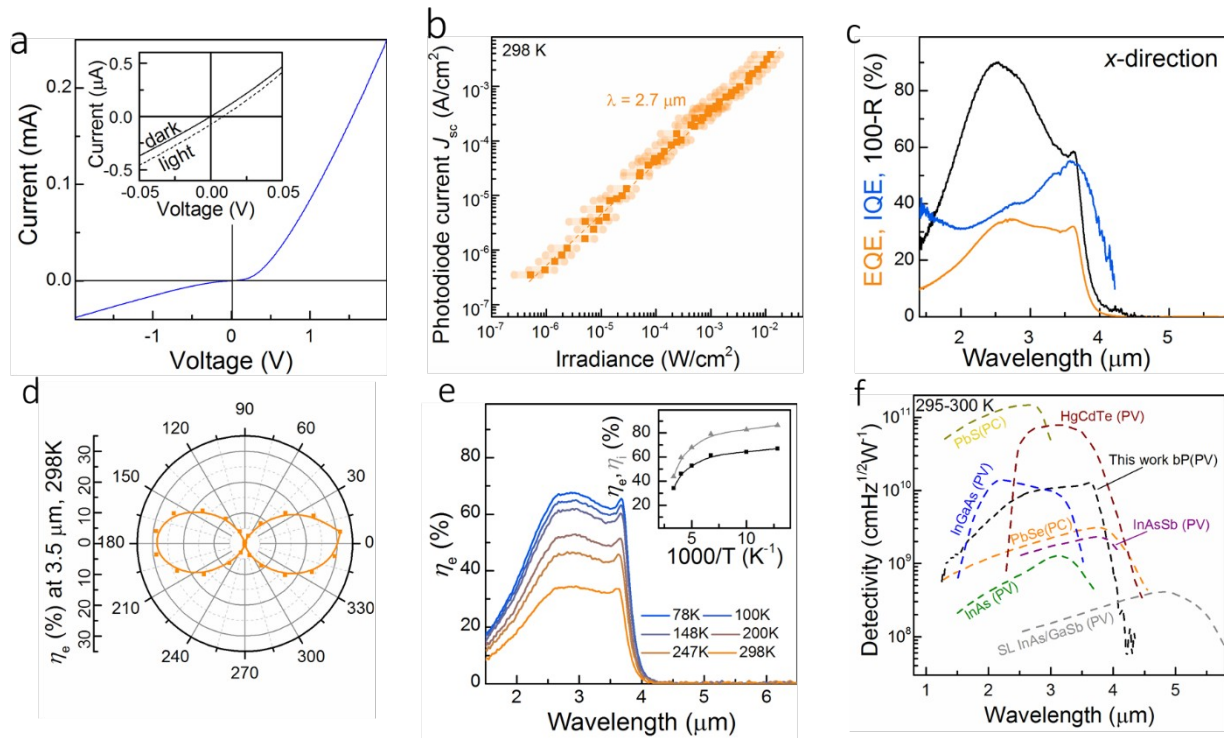
471**Fig. 1 | bP/MoS₂ heterojunction photodiode. a**, Schematic of device 472configuration, showing the heterojunction and contact configuration. **b**, 473Optical micrograph of a completed device, regions containing bP and MoS₂ 474are outlined for clarity. **c**, Simulated energy band diagram of the device 475under equilibrium. **d**, Cross-sectional TEM image of a completed photodiode. 476**e**, High resolution cross-sectional TEM image showing the bP/MoS₂ interface. 477**f**, High resolution cross-sectional TEM image showing the bP/Au interface.

478
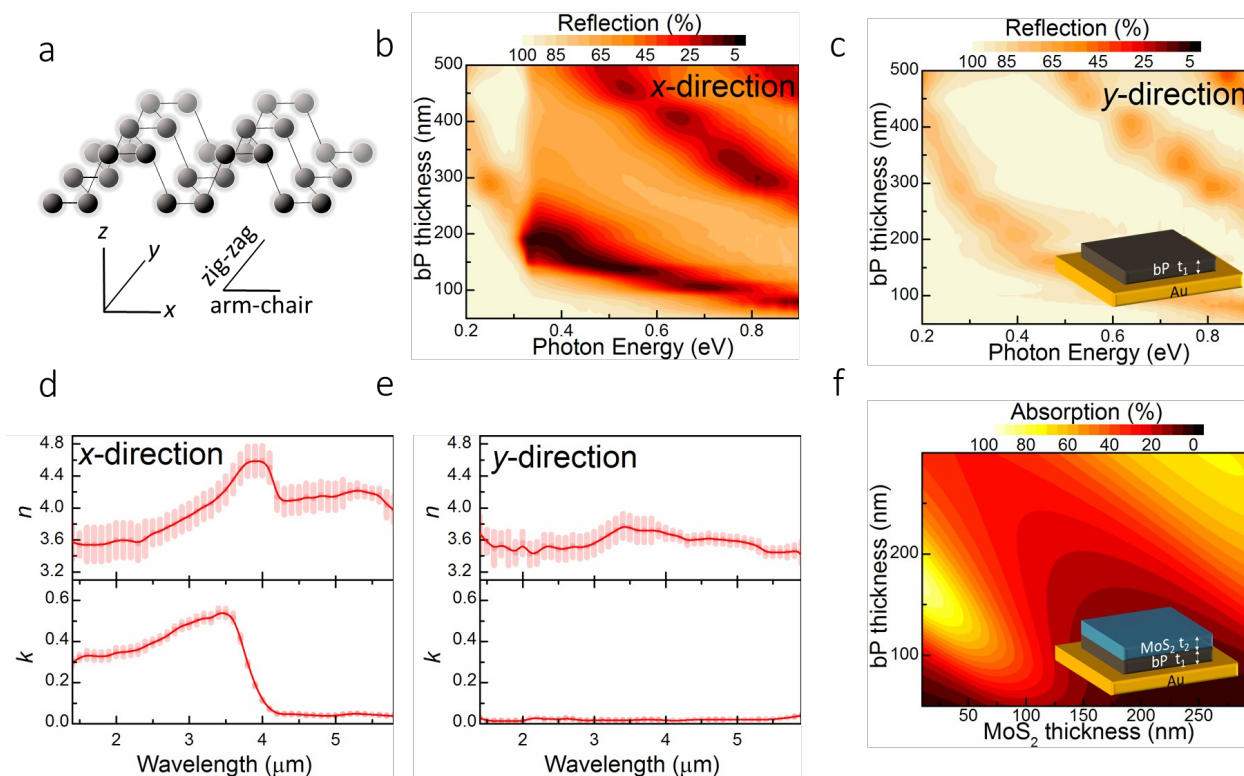
480 Fig. 2 | Infrared optical constants of bP. a, Schematic diagram of bP 481 crystal structure, **b**, Reflection of bP on Au, measured for crystals with 482 thickness ranging from 50 nm to 500 nm with the polarizer aligned in the *x*- 483 direction. **c**, Reflection of bP on Au, measured for crystals with thickness 484 ranging from 50 nm to 500 nm with the polarizer aligned in the *y*-direction. 485 **d**, Extracted complex refractive index of bP in the *x*-direction. **e**, Extracted 486 complex refractive index of bP in the *y*-direction. Error bars in d and e are 487 based on the deviation between the modelled and measured reflection at 488 each wavelength. **f,** Modelled absorption in bP layer, for a bP / MoS$_2$ stack on 489 Au, as a function of the bP and MoS$_2$ layer thicknesses.

490

Fig. 3 | Photoresponse and detectivity. a, *IV* curve of a bP/MoS$_2$
493heterojunction photodiode; inset shows measurement taken in the dark and
494under illumination by a 1000 K blackbody source over a voltage range of V =
495±50 mV. **b**, Measured photocurrent as a function of incident illumination
496intensity. Excitation is performed with a λ = 2.7 μm laser diode. Error bars
497are based on the uncertainty in the laser spot size, **c**, spectrally dependent
498η_e, η_i and 100%-*R* for a bP / MoS$_2$ heterojunction photodiode, **d**, measured η_e
499at λ=3.5 μm as a function of polarization angle, **e**, Spectral η_e as a function
500of temperature. Inset shows η_e and η_i at λ=3 μm as a function of
501temperature. **f**, Specific detectivity as a function of wavelength measured for
502a bP / MoS$_2$ heterojunction at room temperature as well as various
503commercially available and reported MWIR photodetectors. The shaded

504region highlights the MWIR band. All FTIR and laser diode characterization

505was performed at a device bias of 0 V.

Fig. **4** |
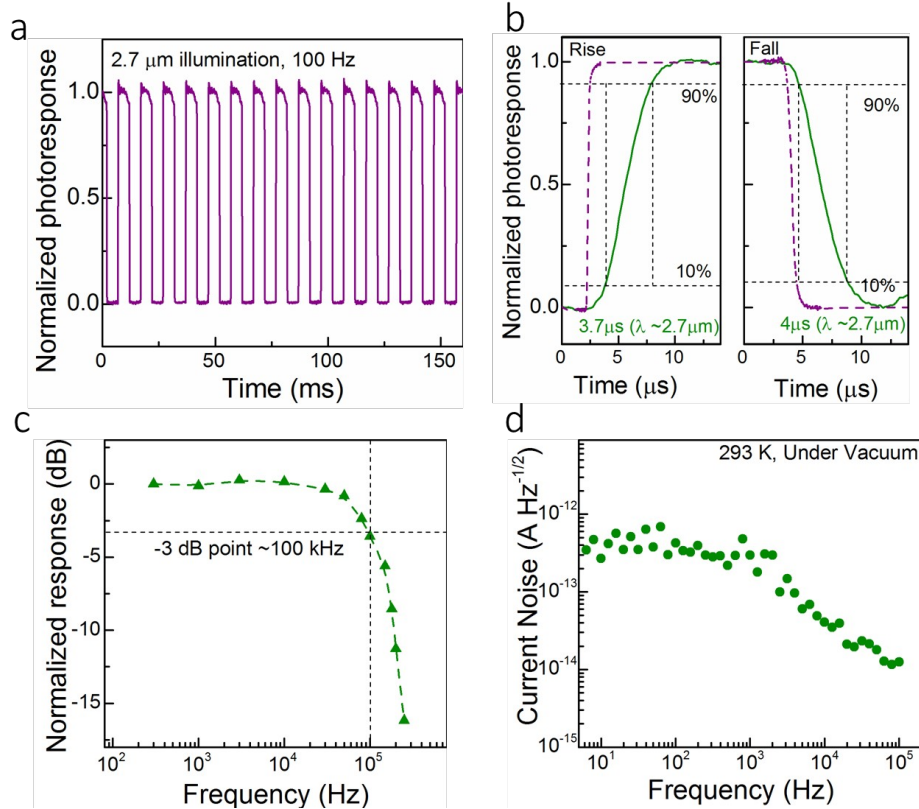
507**Frequency response and noise. a**, Photocurrent measured from a bP / 508MoS$_2$ photodiode under a modulated illumination source (λ= 2.7 μm). **b**, 50990%-10% rise and fall times measured with a λ= 2.7 μm illumination source 510(~10 mW/cm^2). Green solid lines are representative of the bP / MoS$_2$ 511photodiode and the purple dotted lines show the instrument response 512(measured using a commercial InAs photodiode, Judson J12D). **c**, Frequency 513response of a bP / MoS$_2$ photodiode, showing a 3 dB frequency of 100 kHz 514(λ=1.6 μm). **d**, Spectral noise density of a bP / MoS$_2$ photodiode. All device 515photoresponse and noise characterization was performed at a bias of 0 V.

516
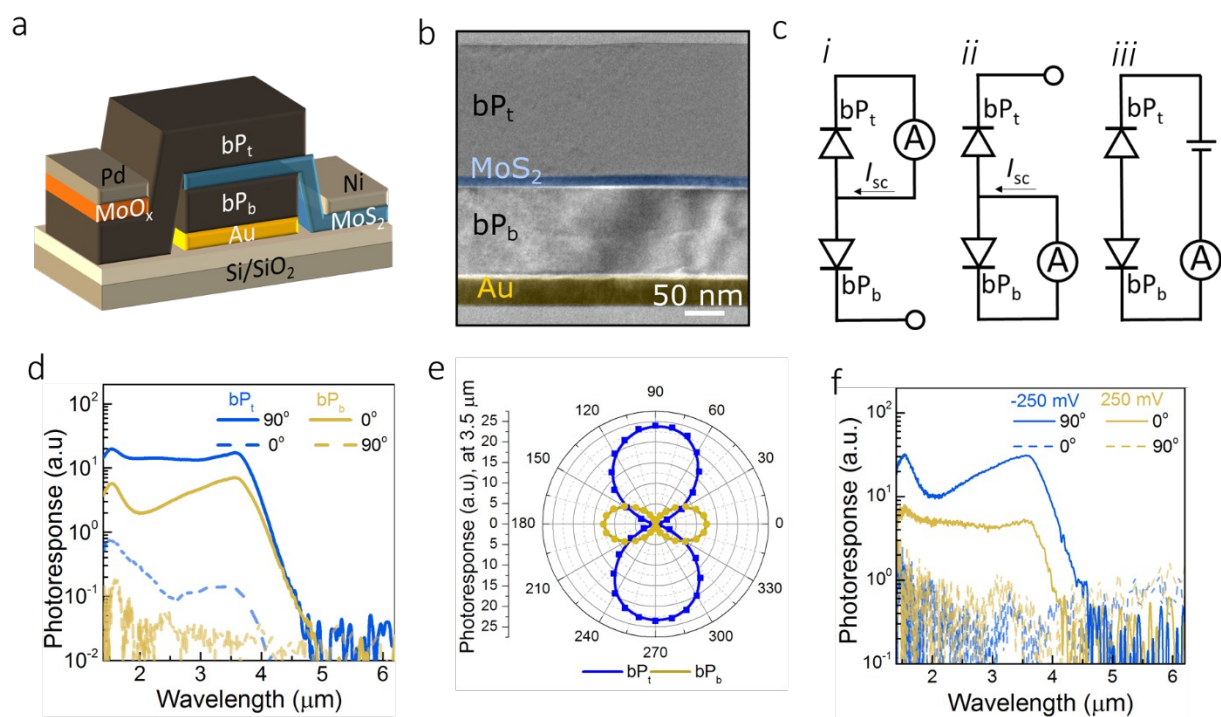
517 Fig. 5 | Polarization resolved bP/MoS$_2$ heterojunction photodiode. a,

518 Schematic of polarization resolved bP/MoS$_2$ heterojunction photodiode,

519 showing the heterojunction and contact configuration. **b**, Cross-sectional TEM

520 image of a completed polarization resolved bP/MoS$_2$ heterojunction

521 photodetector, showing the various layers in the device. **c**, Electrical

522 configurations used to measure: photoresponse from bP$_t$ (i), photoresponse

523 from bP$_b$ (ii), and photoresponse from the top or bottom mode using the bias

524 selectable mode (iii). **d**, Spectrally resolved photoresponse measured from

525 bP$_t$ and bP$_b$ under linearly polarized illumination normal and perpendicular to

526 the device. **e**, Measured photoresponse under linearly polarized illumination

527 at λ = 3 μm in bP$_t$ and bP$_b$ as a function of polarizer angle. **f**, spectrally

528 resolved photoresponse of the device in the bias selectable mode under four

529different conditions: ±250 mV for polarization aligned to the x-axis of the top

530and bottom devices.

531

532 References

533 1. Xia, F., Wang, H., Xiao, D., Dubey, M. & Ramasubramaniam, A. Two-dimensional
534   material nanophotonics. *Nat. Photonics* **8,** 899–907 (2014).

535 2. Jakšić, Z. *Micro and Nanophotonics for Semiconductor Infrared Detectors*.
536   (Springer-Verlag, 2014).

537 3. Rogalski, A., Adamiec, K. & Rutkowski, J. *Narrow-Gap Semiconductor Photodiodes*.
538   (SPIE Press, 2000).

539 4. Wang, X., Cheng, Z., Xu, K., Tsang, H. K. & Xu, J.-B. High-responsivity
540   graphene/silicon-heterostructure waveguide photodetectors. *Nat. Photonics* **7,**
541   888–891 (2013).

542 5. Xia, F., Wang, H. & Jia, Y. Rediscovering black phosphorus as an anisotropic
543   layered material for optoelectronics and electronics. *Nat. Commun.* **5,** 5458
544   (2014).

545 6. Ling, X., Wang, H., Huang, S., Xia, F. & Dresselhaus, M. S. The renaissance of
546   black phosphorus. *Proc. Natl. Acad. Sci.* **112,** 4523–4530 (2015).

547 7. Yuan, H. *et al.* Polarization-sensitive broadband photodetector using a black
548   phosphorus vertical p–n junction. *Nat. Nanotechnol.* **10,** 707–713 (2015).

549 8. Qiao, J., Kong, X., Hu, Z.-X., Yang, F. & Ji, W. High-mobility transport anisotropy
550   and linear dichroism in few-layer black phosphorus. *Nat. Commun.* **5,** 5475
551   (2014).

552 9. Hong, T. *et al.* Anisotropic photocurrent response at black phosphorus–MoS2 p–n
553   heterojunctions. *Nanoscale* **7,** 18537–18541 (2015).

554 10. Deng, Y. *et al.* Black Phosphorus–Monolayer MoS2 van der Waals
555   Heterojunction p–n Diode. *ACS Nano* **8,** 8292–8299 (2014).

556   11.   Ye, L., Li, H., Chen, Z. & Xu, J. Near-Infrared Photodetector Based on
557   MoS2/Black Phosphorus Heterojunction. *ACS Photonics* **3,** 692–699 (2016).

558   12.   Chen, P. *et al.* Gate tunable WSe2–BP van der Waals heterojunction devices.
559   *Nanoscale* **8,** 3254–3258 (2016).

560   13.   Shim, J. *et al.* Phosphorene/rhenium disulfide heterojunction-based negative
561   differential resistance device for multi-valued logic. *Nat. Commun.* **7,** 13413
562   (2016).

563   14.   Huang, M. *et al.* Broadband Black-Phosphorus Photodetectors with High
564   Responsivity. *Adv. Mater.* **28,** 3481–3485 (2016).

565   15.   Youngblood, N., Chen, C., Koester, S. J. & Li, M. Waveguide-integrated black
566   phosphorus photodetector with high responsivity and low dark current. *Nat.*
567   *Photonics* **9,** 247–252 (2015).

568   16.   Guo, Q. *et al.* Black Phosphorus Mid-Infrared Photodetectors with High Gain.
569   *Nano Lett.* **16,** 4648–4655 (2016).

570   17.   Mao, N. *et al.* Optical Anisotropy of Black Phosphorus in the Visible Regime. *J.*
571   *Am. Chem. Soc.* **138,** 300–305 (2016).

572   18.   Liu, H. *et al.* Phosphorene: An Unexplored 2D Semiconductor with a High Hole
573   Mobility. *ACS Nano* **8,** 4033–4041 (2014).

574   19.   Tran, V., Soklaski, R., Liang, Y. & Yang, L. Layer-controlled band gap and
575   anisotropic excitons in few-layer black phosphorus. *Phys. Rev. B* **89,** 235319
576   (2014).

577   20.   Li, D. *et al.* Polarization and Thickness Dependent Absorption Properties of
578   Black Phosphorus: New Saturable Absorber for Ultrafast Pulse Generation. *Sci.*
579   *Rep.* **5,** 15899 (2015).

580   21.   Macleod, A. *Thin-Film Optical Filters*. (CRC Press, 2010).

581 22. Villegas, C. E. P., Rocha, A. R. & Marini, A. Anomalous Temperature

582 Dependence of the Band Gap in Black Phosphorus. *Nano Lett.* **16,** 5095–5101

583 (2016).

584 23. Villegas, C. E. P., Rodin, A. S., Carvalho, A. & Rocha, A. R. Two-dimensional

585 exciton properties in monolayer semiconducting phosphorus allotropes. *Phys.*

586 *Chem. Chem. Phys.* **18,** 27829–27836 (2016).

587 24. Li, L. *et al.* Quantum Hall effect in black phosphorus two-dimensional electron

588 system. *Nat. Nanotechnol.* **11,** 42 (2016).

589 25. Martyniuk, P., Kopytko, M. & Rogalski, A. Barrier infrared detectors. *Opto-*

590 *Electron. Rev.* **22,** 127–146 (2014).

591 26. Dhar, N. K., Dat, R. & Sood, A. K. Advances in Infrared Detector Array

592 Technology. in *Optoelectronics - Advanced Materials and Devices* (InTech, 2013).

593 27. Amani, M., Regan, E., Bullock, J., Ahn, G. H. & Javey, A. Mid-Wave Infrared

594 Photoconductors Based on Black Phosphorous-Arsenic Alloys. *ACS Nano* (2017).

595 doi:10.1021/acsnano.7b07028

596 28. Buscema, M. *et al.* Fast and Broadband Photoresponse of Few-Layer Black

597 Phosphorus Field-Effect Transistors. *Nano Lett.* **14,** 3347–3352 (2014).

598 29. Martyniuk, P. & Rogalski, A. HOT infrared photodetectors. *Opto-Electron. Rev.*

599 **21,** 239–257 (2013).

600 30. Yau, L. D. & Sah, C.-T. Theory and experiments of low-frequency generation-

601 recombination noise in MOS transistors. *IEEE Trans. Electron Devices* **16,** 170–

602 177 (1969).

603 31. Haddadi, A., Dehzangi, A., Chevallier, R., Adhikary, S. & Razeghi, M. Bias–

604 selectable nBn dual–band long–/very long–wavelength infrared photodetectors

605   based on InAs/InAs 1−x Sb x /AlAs 1−x Sb x type–II superlattices. *Sci. Rep.* **7,**

606   3379 (2017).

60732.   Bullock, J., Cuevas, A., Allen, T. & Battaglia, C. Molybdenum oxide MoOx: A

608   versatile hole contact for silicon solar cells. *Appl. Phys. Lett.* **105,** (2014).

60933.   Chuang, S. *et al.* MoS2 P-type Transistors and Diodes Enabled by High Work

610   Function MoOx Contacts. *Nano Lett.* **14,** 1337–1342 (2014).

61134.   Low, T. *et al.* Tunable optical properties of multilayer black phosphorus thin

612   films. *Phys. Rev. B* **90,** 075434 (2014).

61335.   Morita, A. Semiconducting black phosphorus. *Appl. Phys. A* **39,** 227–242

614   (1986).

61536.   Huang, Y. *et al.* An innovative way of etching MoS<Subscript>2</Subscript>:

616   Characterization and mechanistic investigation. *Nano Res.* **6,** 200–207 (2013).